OPEN ACCESS

University of BRISTOL

Peer reviewed version

Link to published version (if available):
10.1016/j.compositesa.2017.10.027

Link to publication record in Explore Bristol Research
PDF-document

University of Bristol - Explore Bristol Research
General rights

Ply-orientation measurements in composites using structure-tensor analysis of volumetric ultrasonic data

L. J. Nelson[a,*], R. A. Smith[a], M. Mienczakowski[a]

[a]*Department of Mechanical Engineering, University of Bristol, Bristol, BS8 1TR, UK*

Abstract

Ply wrinkling in carbon fibre reinforced polymer (CFRP) laminates is often geometrically complex and difficult to quantify using non-destructive techniques. In this paper, an ultrasonic technique for mapping ply wrinkling is presented. The instantaneous-phase three-dimensional dataset obtained from a pulse-echo ultrasonic inspection is processed using the structure-tensor image processing technique to quantify the orientations of the internal plies of a CFRP laminate. It is shown that consideration must be given to the wrapped nature of the phase dataset during processing to obtain accurate orientation maps. Three dimensional ply orientation and ply-location maps obtained from a test coupon are compared with true ply angles and locations by overlaying the ultrasonically-derived results on X-ray CT image slices, showing that accurate orientation maps can be obtained using the proposed technique.

Keywords: A. Layered structures, B. Directional orientation, D. Non-destructive testing, D. Ultrasonics

1. Introduction

1.1. Requirement

In advancing the design of carbon-fibre reinforced polymer (CFRP) laminate components to improve performance and reduce weight, particularly in the aerospace sector, components require precisely controlled and verified fibre and ply structures. For example, it is widely understood that tuning of structural performance is achieved by careful selection of a ply layup sequence, such as the +45°, -45°, 0° and 90° plies of a quasi-isotropic laminate. For clarity in this paper, this in-plane feature of the composite ply is termed '*fibre* orientation' and a local deviation from the desired fibre orientation is termed '*fibre* waviness', as illustrated in Fig. 1(a). Another important geometrical feature of the composite is the out-of-plane orientation of the plies themselves, the planar surfaces which exist as discrete layers on which the fibres are constrained, especially in the context of an out-of-plane wrinkle. This out-of-plane orientation is termed '*ply* orientation', with local deviations from the desired ply orientation referred to as '*ply* wrinkling', as illustrated in Fig. 1(b). The measurement of these ply orientations, and the characterisation of ply-wrinkling defects, together with the mapping of ply locations, are the focus of this paper.
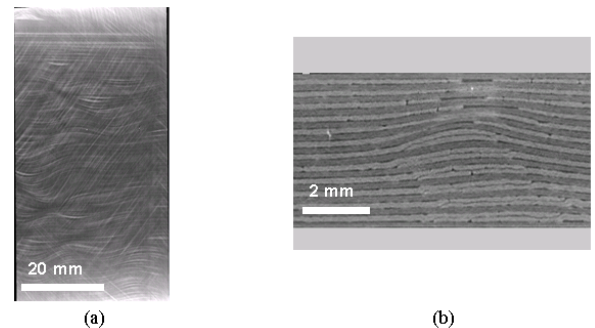

Figure 1: X-ray CT image slices from CFRP laminates showing (a) fibre orientation and evidence of in-plane fibre waviness on an in-plane cross-section, and (b) ply layers and evidence of gaps, overlaps and ply wrinkling on an out-of-plane cross-section.

---

*Corresponding author

Email address: `luke.nelson@bristol.ac.uk` (L. J. Nelson)

Previous research has identified significant effects of ply wrinkling on the compression strength of composites [1, 2]. A recent parametric study using finite-element (FE) analysis by Xie et al. [3] has shown a primary relationship between compressive strength and the wrinkle's maximum angle (ply orientation) to the load direction, with secondary dependencies on wrinkle wavelength and extent as a proportion of component size. Wrinkle angles of 10° resulted in a compressive-strength knock-down factor of over 20%, depending on the cross-sectional area of the wrinkle extent perpendicular to the load direction. The significant strength reduction has drawn attention to this defect type, and continues to drive the need to achieve accurate measurements of maximum wrinkle angle, wrinkle wavelength, and extent using non-destructive methods.

The geometrically complex nature of ply-wrinkling and fibre-waviness defects presents a difficulty for calculating knock-down factors. A growing trend that solves this issue is the use of FE models of as-manufactured components [4–8] with mesh geometries and material properties being derived from the component using non-destructive techniques. In addition to the fibre and ply orientations, FE models require composite-surface and ply locations, thus these are also desired non-destructive outputs. Ply-orientation and ply-location mapping are addressed in this paper. Fibre orientation is the subject of a future paper.

1.2. Candidate non-destructive techniques

X-ray CT provides geometrically accurate 3D imaging of a component making it a desired NDT modality when wishing to image fibre related and ply-related features in 3D space. Much work has been published on using X-ray methods to image and measure such features in fibre-reinforced polymers [9–13] but X-ray CT is not particularly suited to image fibre and ply structure in CFRP composites since the similarity in atomic mass of carbon (fibres) and typical epoxy polymer resin systems produces a low X-ray absorption contrast between these two phases,

making datasets more difficult to analyse. More novel methods have been proposed to overcome this shortfall [14–16] but even then, the physical size of typical aerospace components often precludes inspection using X-ray CT methods because spatial resolution requirements cannot be achieved. In scenarios where X-ray CT is unsuitable, alternative methods are sought. The strongest candidate is ultrasound.

Pulse-echo ultrasound scanning is routinely used in aerospace non-destructive testing of large laminar components. There is a growing desire to extend the use of ultrasound to image ply and fibre features, such as out-of-plane ply wrinkling, in-plane fibre waviness, ply-termination (ply-drop) locations, and ply stacking sequence [17–20]. However, unlike X-ray CT, the raw RF-waveforms from a pulse-echo ultrasonic inspection do not intuitively reveal these features when viewed using 3D volume-rendering techniques, or when processed using the traditional 'gating' methods of signal analysis. Current research into the interaction of ultrasound with layered fibrous composite materials [21] shows how separation of the raw RF signal into its instantaneous phase, amplitude and frequency components is beneficial for observing these features.

It is the objective of this paper to demonstrate that ultrasonic instantaneous-phase data can be analysed using image-processing algorithms to produce 3D maps of ply orientations. These orientation maps can be used for imaging and quantifying ply-wrinkling defects and also as inputs for FE model generation. The use of the phase dataset to further determine composite-surface and ply locations, again for FE model generation, is also demonstrated.

1.3. Paper overview

Firstly, a background section introduces relevant recent progress in analytical modelling of the interaction of ultrasound with layered composite structures which has made this work possible. Then a review of image-processing

techniques capable of quantifying local ply orientation from ultrasonic phase datasets is presented in which the 'structure tensor' is identified as a technique with many potential advantages.

The experimental work in Section 3 describes the CFRP test coupon, ultrasound data acquisition and processing. A new strategy to correctly align, scale and segment the ultrasonic phase data prior to orientation analysis is presented. Without this stage, surface locations, ply locations and ply orientations are potentially distorted.

Section 4 describes the analysis of this phase data using the structure-tensor method. Consideration is given to the wrapped nature of the data. Methods to correctly smooth and calculate gradients in the phase data are presented which allow analysis without causing bias or uncertainty in the orientation results. In Section 5 the effect of the structure-tensor parameters on the resulting orientation maps are explored. With optimised parameters, the combined ply-orientation and ply-location map is visualised using vector lines overlaid on an X-ray CT image slice from the coupon, confirming correlation with the real structure. A summary and discussion of the main conclusions are given in Section 6.

2. Background

2.1. Ultrasonic interaction with layered fibrous composite materials

An analytical model [17, 22] that predicts the response of layered composite structures to normal-incidence plane-wave ultrasound has demonstrated that, by using a probe with a centre frequency close to the resonant frequency of the plies, it is possible to enhance the reflections from the thin inter-ply resin layers that are present between plies in the composite stack (Fig. 2).

With input-pulse characteristics that excite the fundamental ply resonance, the instantaneous phase increases by 2π radians for each ply traversed in the bulk of the
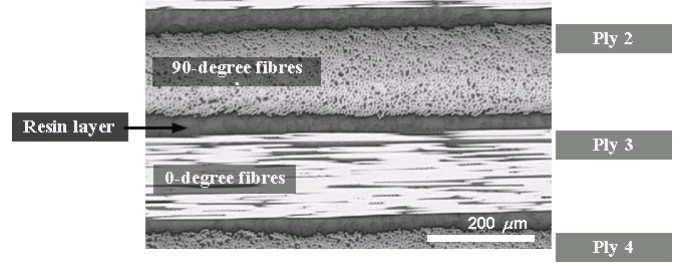

Figure 2: Optical micrograph of the resin layers that exist between composite plies. In this case, the resin layers contain thermoplastic toughening particles, causing increased resin-layer thickness.

material [21]. Model predictions show that the phase attains a value of $\phi_0 - \frac{\pi}{2}$ radians at each resin-layer location, where ϕ_0 is the input-pulse phase at peak amplitude and can be determined adequately from the front-surface reflection. At the front and back surface of the composite stack, phase values of ϕ_0 and $\phi_0 - \pi$ are observed at the peaks in instantaneous amplitude arising from those interface reflections.

Probe frequency and bandwidth characteristics play a vital role in obtaining a response from the composite that retains sensitivity to ply location throughout the composite stack [17, 21, 23]. For example, the probe's centre frequency must be close to the resonant frequency of the composite plies, which is typically around 6 MHz for 0.25 mm plies, and 8 MHz for 0.189 mm plies. Further, the probe must also have a broad-band pulse so that plies that vary in thickness (a consequence of ply wrinkling) still exhibit resonant frequencies that fall within the frequency response range of the probe. Typically a bandwidth approximately equal to the centre frequency (a Q-factor of 1) is sought [17].

Once a pulse-echo ultrasound scan has been acquired in which the instantaneous phase has sensitivity to ply locations, attention can move to inversion: extracting the ply-orientation information present in the 3D dataset. For this purpose, texture-orientation image-processing algorithms are required.

3

2.2. Orientation measurement techniques

A number of techniques exist for evaluating local orientation in image data, spanning many scientific fields. Three broad categories of techniques used to obtain such orientation maps are: matched-filter methods, image-transform methods, and gradient methods.

Matched-filter methods employ oriented filters [24] which are tuned to match the features to be detected. The orientation of the filter providing maximal response defines the local orientation. These methods have found uses in many fields including texture analysis [25], digital hair modelling [26], and quantifying 3D fibre and ply orientations in CFRP laminates [20, 27–33].

Image-transform methods rely on transforming the image into a new form, from which the orientations of features are more readily extracted. Two transforms suitable for this purpose are the 2D fast Fourier transform (2D FFT) and Radon, or related Hough, transforms. Uses of the FFT method include fibre orientation [34–37] and ply orientation [19]. Radon transforms have successfully been used for orientation analysis of retinal vessels [38], textures [39, 40], fibres and plies [7, 41]. Whilst these transform methods are preferred over the matched-filter methods for instantaneous-phase data [7, 18] it is the final class of gradient-based methods that are believed to be most promising in this application.

Gradient methods [42, 43] rely on the rate of change of grey level with distance in a particular direction in a greyscale or intensity image. This is useful because gradient is a maximum in a direction perpendicular to the edge of a feature, such as a line in 2D, or plane in 3D. The 'structure tensor' method [44–47] is a gradient-based method that is used in a diverse range of applications. This technique is thought to be particularly suitable because the instantaneous-phase dataset from a laminar CFRP composite is dominated by a phase gradient that is locked to the ply structure, thus it is selected above the other methods for use in this study.

2.3. Structure-tensor formulation

Image gradients, and how these gradients vary over a local region, form the underlying principle of the local structure tensor. A structure tensor, $\mathbf{S}$, is calculated for each 3D image pixel by first smoothing the image, I, using a smoothing kernel, G_σ, followed by calculation of gradients, typically using central-difference kernels, in three orthogonal directions to yield I_x, I_y and I_z. The tensor is constructed from gradient products, see Eq. (1). A second smoothing kernel, G_τ, defines the smoothing applied to each tensor element.

$$\mathbf{S} = G_\tau * \begin{bmatrix} I_x^2 & I_x I_y & I_x I_z \\ I_x I_y & I_y^2 & I_y I_z \\ I_x I_z & I_y I_z & I_z^2 \end{bmatrix} \tag{1}$$

The smoothing kernels G_σ, and G_τ, are 3D Gaussian kernels with standard deviations σ, and τ, respectively. The parameter σ defines the 'inner scale' or 'smoothing scale' and is set to pre smooth the image to supress noise, but at a scale appropriate to retain local features of interest. The parameter τ defines the 'outer scale' or 'integration scale'; it governs the scale over which the spatial average of the tensor's components are obtained and ideally is selected to average over a region in which the orientation is expected to remain constant such that orientation-noise is smoothed at a scale appropriate to the image structure.

The eigenvectors (principal gradient directions) v_1, v_2 and v_3 of each tensor hold information about the structure's orientation, whilst the associated eigenvalues λ_1, λ_2 and λ_3 (where $\lambda_1 > \lambda_2 > \lambda_3 > 0$), can be used to determine the class of structure present. Three classes of structures can be identified (spherical, linear or planar) based on the eigenvalues [48, 49] as described below and depicted pictorially in Fig. 3.

1. Spherical/isotropic structure ($\lambda_1 \approx \lambda_2 \approx \lambda_3$): there is no preferred orientation and the local image structure is isotropic with spherical symmetry.

2. Linear structure ($\lambda_1 \approx \lambda_2 \gg \lambda_3$): the gradient along the direction of alignment (of rods, for example) is low

whilst, in the two orthogonal directions, a high gradient is detected. The linear axis is parallel to the eigenvector associated with the *smallest* eigenvalue (λ_3).

3. Planar structure ($\lambda_1 \gg \lambda_2 \approx \lambda_3$): in a direction perpendicular to the planes, the gradient is high, whilst the two in-plane gradients are low. The plane-normal is given by the eigenvector associated with the *largest* eigenvalue (λ_1).

In Fig. 3, the tensor for each class is visualised as an ellipsoid whose orientation corresponds to the eigenvectors, and radius is given by the eigenvalues which quantify the gradient in that direction. It is possible, based on the relative magnitude of the eigenvalues, to quantify the degree to which a local region conforms to these three classes of structure [49]. Eq. (2), (3) and (4) give spherical, linear and planar anisotropy metrics (c_s, c_l and c_p respectively). Each of these metrics is bounded between zero and one, and their sum is equal to one.

$$c_s = \frac{\lambda_3}{\lambda_1} \tag{2}$$

$$c_l = \frac{\lambda_2 - \lambda_3}{\lambda_1} \tag{3}$$

$$c_p = \frac{\lambda_1 - \lambda_2}{\lambda_1} \tag{4}$$

A key feature of this tensor-based approach is that antipodal vectors are mapped onto identical tensor representations, thus allowing vector averaging without cancellation of opposing-direction vectors. This property, as well as the classification capability, has driven the popularity of the structure-tensor method. Examples of its use include determination of 3D fibre orientation in composites such as GFRP, CRC and C/SiC [50], as well as wood-fibre composites [51] and many biomedical fields [52, 53]. The 3D planar nature of structures assessed in the seismology field [54, 55] is particularly relevant to this current work. The application of this structure-tensor method to ultrasonic
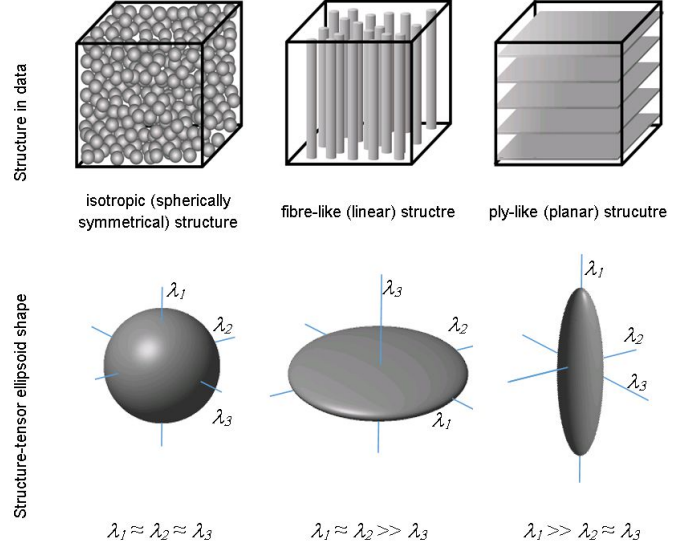

Figure 3: Examples of three classes of structure in 3D data (above) and the corresponding structure-tensor shape when viewed as an ellipsoid (below).

pulse-echo NDT data has not been reported previously in the scientific literature. This paper reports its novel application to ultrasonic instantaneous-phase data and shows how adverse phase-wrapping and aspect-ratio effects can be avoided.

3. Ultrasonic data acquisition and processing

3.1. CFRP sample details

The carbon-fibre laminate studied in this paper was manufactured from an IMA/M21 carbon-fibre/resin prepreg system. The cross-ply $[(0/90)_6/\overline{0}]_s$ laminate comprises 25 unidirectional plies at 189 µm spacing. The interply resin-layer thickness was estimated, from micrograph analysis, to be approximately 40 µm, so the composite plies themselves are approximately 149 µm thick. These thick resin layers produce strong ultrasonic reflections thus giving a high signal-to-noise ratio [22]. The authors' experience with fibre-resin systems exhibiting thinner resin layers shows that, although these produce weaker reflections, sufficient signal is obtained to allow the orientation measurement techniques described in this paper to be applied [56]. Out-of-plane wrinkles in the 0° direction were

5

induced through a process of introducing tape overlaps and gaps in the 90° plies at specific locations [57]. During cure there is vertical movement of plies tending to create a uniform fibre volume fraction resulting in predictable wrinkling in the cured composite, as seen in the X-ray CT cross section in Fig. 4.
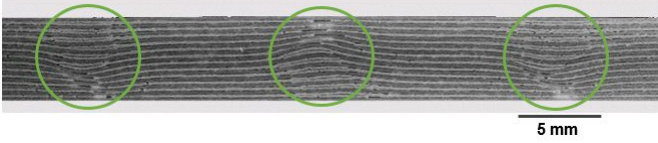

Figure 4: Cross section through an X-ray CT data volume from the CFRP laminate used in this paper with the three wrinkle zones highlighted. The darker plies have fibres in the plane of the paper – corresponding to 0°.

3.2. Ultrasonic pulse-echo data acquisition

Modelling of the composite structure using the analytical model in [21, 22] was used to determine the optimised data-acquisition parameters. The resonant frequency of the 189 μm ply spacing is calculated by the model to be 7.9 MHz. The closest frequency of commercially-available ultrasonic probe has a specified centre frequency of 7.5 MHz. For the inspection, a 7.5 MHz Olympus Videoscan probe, with a measured centre frequency of 6.6 MHz and -6 dB bandwidth of 5.6 MHz , was used. The probe, which had a 12.5 mm diameter active element with a focal distance of 38 mm in water, was mounted in an ultrasonic immersion scanning tank such that the probe's focal plane was at the mid-plane of the composite laminate. Received waveforms were digitised at 125 MHz sampling frequency and recorded at a 0.2 mm scan pitch in the x and y directions.

3.3. Instantaneous amplitude and phase

Once digitised, the Hilbert transform was used to obtain the analytic signal of each pulse echo waveform acquired from the scanning system [17]. From this, the instantaneous-amplitude and instantaneous-phase datasets were generated. Although only the phase data is used in

orientation analysis, amplitude data is required to perform the alignment and segmentation pre-conditioning stages, which are described below.

3.4. Alignment and segmentation

Sample misalignment during scanning, and the dissimilar sound velocities in the coupling medium and component, can lead to errors in measured surface locations and ply-location mapping (and therefore ply orientations), so it must be corrected for appropriately. The corrections all depend on precise measurement of the front- and back-surface times-of-flight in the waveform. In conventional ultrasonic inspection, this is most commonly achieved by detecting a peak or a threshold-crossing in the unrectified waveform. Fig. 5(a) presents an unrectified 'B-scan' (cross section) through the ultrasonic full-waveform data in which the front surface and rear surface can be easily identified by the high-amplitude reflections that occur at these times of flight. However, peak-detection methods for unrectified raw waveforms are not always sufficiently accurate for the current purposes, particularly in the presence of ply wrinkling and ply drops. A new method is presented that, instead of using the raw unrectified waveform, uses a combination of instantaneous-amplitude and phase data to provide the time-of-flight accuracy required for use in data alignment, segmentation and orientation measurement.

Initially, instantaneous-amplitude data is used to define the front- and rear-surface locations (in time) because the peak instantaneous amplitude has been shown by modelling to coincide with the time-of-flight to these interfaces. Whilst this gives an accurate front-surface location, the rear-surface location can exhibit a high degree of variability, particularly when the signal is disrupted due to ply wrinkling, ply drops, tape gaps and overlaps. This is the case for the CFRP laminate studied in this paper, as seen in Fig. 5(b) - an instantaneous-amplitude cross-section (in dB relative to the front-surface reflection amplitude) where the red lines indicate the times-of-flight to the front- and
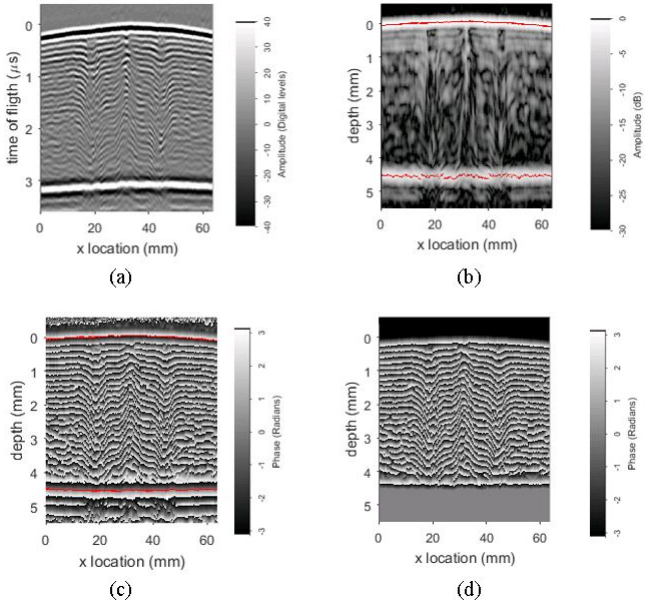
Figure 5: Cross sections through the ultrasonic data at a common x-z plane showing (a) the raw waveform, (b) instantaneous amplitude with red lines indicating surface locations measured from amplitude peaks, (c) instantaneous phase with red lines indicating surface locations measured from the phase data, and (d) segmented phase data suitable for structure-tensor assessment.

rear-surface peak amplitudes. In these scenarios it is possible to increase the robustness of the back-surface location in the data by using phase data, as follows.

Modelling predictions [21] show that the front surface exhibits a phase of ϕ_0, whilst the phase at the back surface is $\phi_0 - \pi$, where ϕ_0 is the phase at peak amplitude of the input pulse. An estimation of ϕ_0 is made using the front-surface reflection by calculating the mean phase at the peak instantaneous amplitude, averaged across a region of the scan. For the probe and experimental setup used in this study, ϕ_0 was measured to be 3.19 radians. The rear surface is thus expected to exhibit a phase of 0.05 radians. A search is made in the vicinity of the front-surface and rear-surface peak amplitudes to find the nearest digitisation point to these characteristic phase values. Using this instantaneous-phase method, the front-surface time-of-flight strongly agrees with the peak-amplitude time-of-flight, whilst the rear-surface measurement is improved,

appearing much smoother than the amplitude-derived value, as seen in Fig. 5(c). In this figure the red lines represent the surface location measured from the phase data.

Surface-location measurements identified that the sample's front surface was curved, and also slightly inclined to the scanner's x-y plane. This can be seen in the raw B-scan cross-section in Fig. 5(a). It is a requirement to correct for the misalignment to the scanner axes and the curvature of the front surface differently, for reasons that will become clear.

Misalignment is conventionally corrected using an 'interface gate', either at acquisition time or later during analysis. The interface gate detects the first crossing of an amplitude threshold and time-shifts each waveform to synchronise that time-of-flight across the whole scan, creating a flat front-surface signal. However, in cases where a sample has a curved or wrinkled front surface, this is not appropriate because forcing the surface to become planar propagates the inverse of the surface undulations into the ultrasonic data that follows, leading to ply-orientation and ply-location errors. To avoid this, the predicated front-surface location has been used to calculate a plane-of-best-fit to the surface, which is used to time-shift each A-scan so that the front surface lies nominally in the x-y plane, but retains its curvature. This proposed alignment method will be required for all components that have a non-flat front surface when scanned in immersion.

An additional consideration for curved or wrinkled surfaces is the dissimilar velocities in the coupling medium (water), and the material being inspected (CFRP). The effects on the raw data are to exaggerate (by a factor of approximately two in this case) the surface undulations, and superimpose them on data at later times-of-flight, resulting in wrinkle or curvature 'artefacts' in the B-scan data. To give a true image of the component's ply structure it is important to apply the correct velocity to each portion of the waveform, using the measured front-surface location to separate them. The benefit can be seen when

comparing the raw-waveform cross-section before correcting for the velocity mismatch, Fig. 5(a), with Fig. 5(b)-(d) in which the velocity correction has been applied. In this paper, velocities of 1480 ms^{-1} and 3043 ms^{-1} were used for the water and composite respectively.

This alignment and velocity-correction process is important for obtaining geometrically accurate and aligned datasets so that accurate surface locations, ply locations and ply orientations can be measured, and comparisons can be made to similarly-aligned X-ray CT datasets.

The next stage is segmentation to exclude phase data before the front surface, and after the rear surface, because the phase still increases with time in these regions, despite the low amplitudes, and can affect the structure-tensor method. With the surface locations known, it is a simple task to replace these regions with a single uniform phase value outside the sample bounds. A phase value of ϕ_0 is assigned to data before the front surface, and $\phi_0 - \pi$ to data after the back surface. Segmenting the data in this way, as seen in Fig. 5(d), avoids high gradients at the surfaces, which would otherwise bias the structure-tensor measurement near these locations.

The three-dimensional aligned, scaled and segmented phase data, Φ, a cross section of which is shown in Fig. 5(d), clearly shows ply structure with the three wrinkle zones at x-locations of 20 mm, 30 mm and 45 mm, and is now suitable for orientation analysis using the structure-tensor method, and ply-location analysis using phase tracking.

4. Structure-tensor analysis of instantaneous-phase data

Applying the structure-tensor method to instantaneous-phase data requires careful consideration because the phase is a 'wrapped' dataset, in this case taking values in the range $-\pi$ to $+\pi$ radians. In each ply, the phase is predicted to achieve a 2π rotation so, once per ply there has to be a -2π 'step' as shown in the cross-section though

a wrinkled composite simulated in Fig. 6(a). This effect must be dealt with correctly in the pre-smoothing process, and during gradient calculations, to avoid erroneous structure-tensor output as in Fig. 6(b) and so that accurate orientation maps can be obtained, Fig. 6(c).
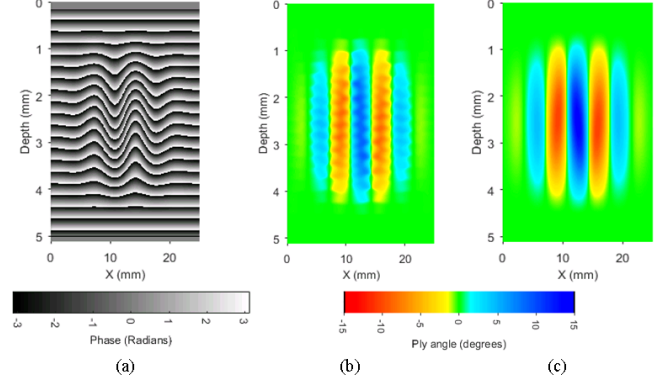

Figure 6: Results from a simulated ultrasonic instantaneous-phase dataset from a composite laminate exhibiting ply wrinkling. The cross section in (a) shows the instantaneous-phase response. A ply angle map measured using the structure-tensor process without accounting for the phase wrap is shown in (b), and after correctly accounting for it in (c).

To smooth (average) the wrapped instantaneous-phase 3D dataset it is first converted into real (Φ_{cos}) and imaginary (Φ_{sin}) components of complex numbers on the unit circle at each phase angle. These components are convolved with the Gaussian smoothing kernel G_σ, then recombined using the inverse tangent function to yield the smoothed wrapped phase dataset Φ_σ.

The second stage at which the wrapped nature of the data needs to be considered is the calculation of phase gradients (Φ_x, Φ_y, Φ_z) from the smoothed wrapped-phase data. If unaccounted for, the large gradient associated with wrap locations dominates measured orientations and introduces errors such as the periodic variations seen in Fig. 6(b). To avoid this, again it is necessary to use the real and imaginary components of the unit-magnitude complex value, as these are continuous functions from which gradients can be calculated by convolution with appropriate kernels. The chain rule is used to obtain the following

general expression for the rate of change of phase (instantaneous frequency), in this case in the x-direction:

$$\phi_x = \frac{\partial \phi}{\partial x} = \cos^2 \phi \frac{\partial \tan \phi}{\partial x} \qquad (5)$$

However, $\tan \phi$ is also a discontinuous function so it needs to be expressed in terms of the continuous sine and cosine functions, which have already been calculated. Then the quotient rule gives the following expression for the phase gradient:

$$\phi_x = \cos \phi \frac{\partial \sin \phi}{\partial x} - \sin \phi \frac{\partial \cos \phi}{\partial x} \qquad (6)$$

Eq. (6) allows calculation of unwrapped phase gradients directly from the wrapped phase, without having to first unwrap the phase, a process that is notoriously inconsistent for experimental data. The required derivatives in Eq. (6) are calculated by convolving the sine and cosine of the smoothed phase 3D dataset, Φ_σ, with $3 \times 3 \times 3$ central-difference Scharr kernels operating in the x, y and z directions to yield the phase-gradient tensor components Φ_x, Φ_y and Φ_z.

The final consideration of the phase data is the non-uniform aspect ratio associated with ultrasonic 3D datasets with two spatial axes (x and y) and one time axis converted to depth (z) using the acoustic velocity as described in Section 3.4. Thus it is important that phase gradients are scaled correctly in units of phase-per-millimetre to ensure correct angular measurements are obtained from the structure-tensor process. The scaled phase-gradients Φ_x, Φ_y and Φ_z are used to construct a structure tensor, Eq. (1), for each (x, y, z) pixel location, from which the eigenvalues and eigenvectors are obtained to reveal structural and orientation information.

5. Results and visualisation

5.1. Instantaneous phase as a map of ply interfaces and sample surfaces

To confirm that the instantaneous-phase data maps the ply structure accurately, the locations of the front surface, rear surface and resin-layer characteristic phases (Section 3.4) have been combined into the interface map shown in Fig. 7. In this figure, red lines are the sample surfaces, whilst blue lines indicate resin layers between plies. These lines are overlaid on a greyscale X-ray CT slice.
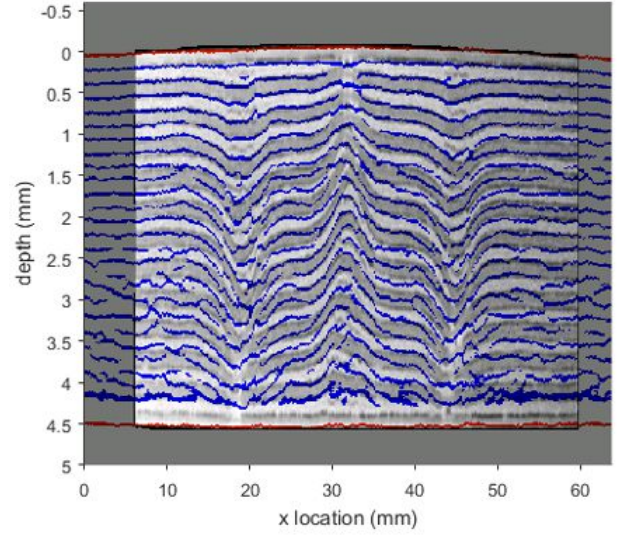

Figure 7: The ultrasonic-phase derived surface and interface map (red and blue respectively) overlaid on composite internal structure as determined from X-ray CT (greyscale).

The image in Fig. 7 shows that the ultrasonic phase has the potential to map ply interfaces, and position them correctly in the majority of locations. This type of information can be used for the generation of FE meshes of as-manufactured structures. There are some locations, typically towards the rear surface of the component, where the phase prediction is not perfectly correlated with the CT image data. This will need to be addressed in the context of FE-mesh generation. However, for the aim of measuring wrinkle angles, the precise location of interfaces is not critical. Also, small and localised deviations in the phase data can be tolerated because the structure-tensor method applies a degree of spatial averaging. Therefore, this analysis provides confidence that the ultrasonic instantaneous-phase data can be processed using the structure-tensor method in order to quantitatively characterise the ply-

wrinkling defects present.

5.2. Application of the structure tensor to instantaneous phase to determine ply orientation

Application of the structure-tensor method to the ultrasonic phase dataset, Fig. 5(d), was performed using MATLAB. The 3D structure tensor centred at each image pixel was calculated, and eigenvalues and eigenvectors for each tensor were computed. For planar structures, such as the ply structure in the example dataset, the eigenvector associated with the largest eigenvalue is the plane's normal vector. The other two eigenvectors lie in a plane perpendicular to the normal vector and their associated eigenvalues were used to calculate the planar anisotropy metric c_p, Eq. (4), which scales from zero to one, and indicates the degree to which the local structure conforms to ply-like (planar) structure.

5.3. Results visualisation using HSV colour-space

Visualisation of the resultant 3D vector data from the 3D volume is not simple. Visualisations become easier as the dimensionality of the data is reduced, and one method is to take cross-sections through the data. Three such cross-sections from the same location in the sample are presented in Fig. 8(a)-(c). These show the ply angle relative to an x-z slice-plane and the x-axis, the associated planar anisotropy metric, and the phase data slice from which they were derived. Combined visualisation of these three images is possible using the hue-saturation-value (HSV) colour space, shown in Fig. 8(d).

In the HSV colour space, ply angle is mapped to the hue (colour) channel, planar anisotropy to the saturation channel, and the phase data to the value (brightness) channel. Allocation of the data channels in this way visually excludes angular measurements from regions where the local structure is not planar, possibly due to noise or an underlying defect in the composite, by mapping these low planar anisotropy values to zero colour saturation. Structural context is given by the phase data, which appears
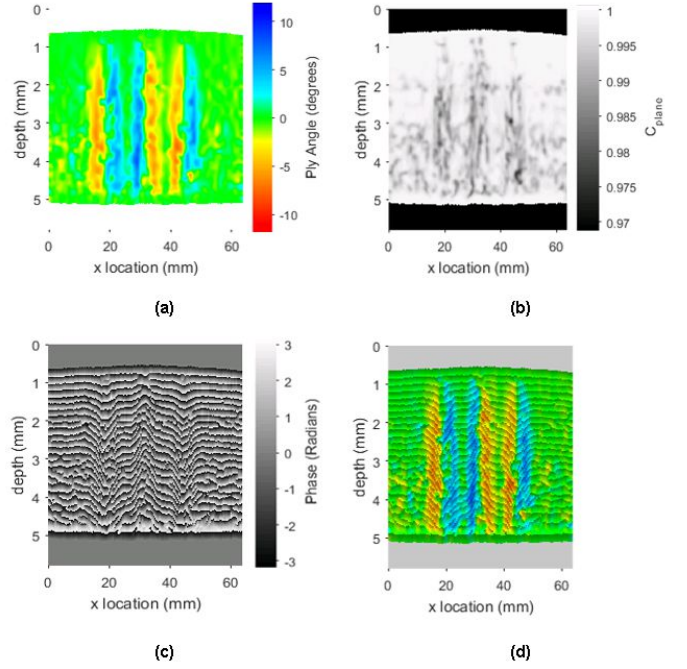

Figure 8: Three separate channels of data; (a) ply angle (hue), (b) planar anisotropy (saturation), (c) instantaneous phase (value), and (d) the combined HSV image. Structure-tensor settings: smoothing scale (0.3, 0.3, 0.019) mm, or (1.5, 1.5, 1.5) pixels; integration scale (0.6, 0.6, 0.038) mm, or (3, 3, 3) pixels.

superimposed. It is clear from the image in Fig. 8(b) that lower planar anisotropy is associated with regions in which the ply angle changes rapidly although, even in these regions, the planar anisotropy is still very close to 1. Therefore, when mapping to the HSV colour space, Fig. 8(d), full colour saturation of the ply-angle occurs everywhere in the image.

An alternative method to compare the structure-tensor result with the true ply angles is to plot vector lines on a 2D slice, and to overlay onto the phase data, or the true structure obtained from X-ray CT. Both HSV and vector-line visualisations are used in the following sections to assess the effect of smoothing scale and integration scale on the measured orientations.

5.4. Effect of smoothing scale

A beneficial feature of the structure-tensor method is the ability to tune the spatial fidelity of the orientation

measurement through the smoothing and integration kernels, the spatial scales of which are determined by the standard deviations σ and τ respectively. Whilst a formulaic method for the selection of these parameters is possible, based on the expected rate of change of ply orientation and the type and level of noise present, this is beyond the scope of this paper. The purpose here is to visually and semi-quantitatively demonstrate the optimum for the example dataset being analysed.

The structure-tensor technique makes pixel-by-pixel gradient measurements, and uses these to determine ply orientation at a very local scale. Therefore, noise in the data can be an influencing factor, so a degree of smoothing is desirable prior to gradient calculation. This is controlled by the smoothing scale, σ, for which there is an optimum value based on the desire to smooth noise without unduly smoothing structural features, so that accurate local orientations are obtained.

Fig. 9 shows the effect of the smoothing-scale standard deviation, σ, on the orientation map for a fixed integration scale τ of (0.6, 0.6, 0.037) mm, or (3, 3, 3) pixels in x, y and z respectively. In this figure, colours indicate ply angle using the colour scale in Fig. 8(a).
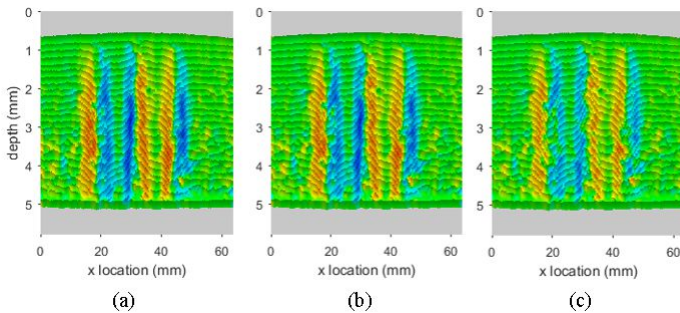

(a)   (b)   (c)

Figure 9: HSV images showing the effect of smoothing scale, σ, on orientation maps for a common B-scan cross-sectional slice. (a) No smoothing (b) σ = (0.2, 0.2, 0.012) mm, or (1, 1, 1) pixels, (c) σ = (0.4, 0.4, 0.024) mm, or (2, 2, 2) pixels. The integration scale, τ, was set at (0.6, 0.6, 0.037) mm, or (3, 3, 3) pixels, in all cases. For ply-angle colour scale, see Fig. 8(a).

The most notable effect of the smoothing scale is an underestimate of ply-angle deviation from horizontal where the ply orientation changes within the region encompassed by the smoothing kernel. Maximum wrinkle angles of approximately ±9° in the un-smoothed and σ = (0.2, 0.2, 0.012) mm cases are measured, but this reduces to approximately ±6° in the σ = (0.4, 0.4, 0.024) mm case. Peak angles measured manually from the CT and ultrasonic-phase data are in the region of ±12°, demonstrating the significant effect this parameter has on the measured angle. A second effect is on the planar anisotropy metric, which increases with increasing smoothing scale, but still remains very high, above 0.97, even with no smoothing. Since accurate measurement of maximum wrinkle-angle is key, and image noise does not appear to have an unduly influencing effect for this data set, smoothing is not required prior to the calculation of image gradients, as in Fig. 9(a).

5.5. Effect of integration scale

The second scale factor, the integration scale, τ, is used to reduce the sensitivity of angular measurements to local noise in the data by increasing the size of the region over which local gradient products are assessed. A value too small will result in sensitivity to small features in the data and lead to larger random errors. A value too large may include gradient measurements from adjacent dissimilar-orientation regions, thus increasing bias and systematic errors, resulting in a greater underestimate of the maximum wrinkle angle. Therefore, an optimum value for the integration scale should exist.

Fig. 10 shows the effect of varying the integration scale for the case where the smoothing scale is set to zero. In this figure, colours indicate ply angle using the colour scale in Fig. 8(a). These images show that, for a large integration scale (Fig. 10(c), τ = (1.0, 1.0, 0.061) mm, or (5, 5, 5) pixels), a smoothly varying orientation map is obtained, but this is at the expense of an underestimate of the maximum wrinkle angle, measured at ±7°, compared with ±12° measured manually from the X-ray CT data.

11

As the integration scale reduces (Fig. 10(b), $\tau = (0.4, 0.4, 0.024)$ mm, or $(2, 2, 2)$ pixels), the measured maximum wrinkle angle of $\pm10°$ approaches the true value but, if the integration scale is set too small (Fig. 10(a), $\tau = (0.2, 0.2, 0.012)$ mm, or $(1, 1, 1)$ pixels), the angular measurement becomes too localised, and the expected smoothly varying orientation map is lost in random variations.
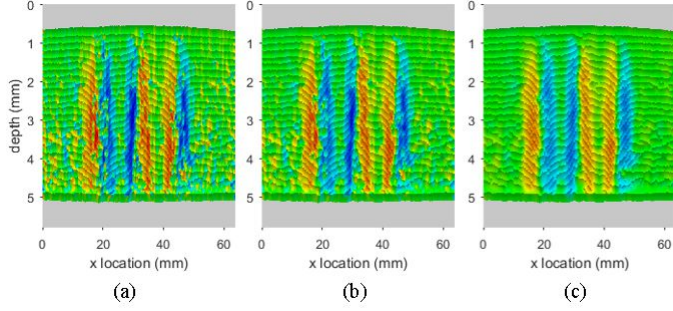

Figure 10: HSV images showing the effect of integration scale, τ, on orientation maps for a common cross-section. (a) $\tau = (0.2, 0.2, 0.012)$ mm, or $(1, 1, 1)$ pixels, (b) $\tau = (0.4, 0.4, 0.024)$ mm, or $(2, 2, 2)$ pixels, (c) $\tau = (1.0, 1.0, 0.061)$ mm, or $(5, 5, 5)$ pixels. The smoothing scale, σ, was set to zero (no smoothing) in all cases. For colour scale see Fig. 8(a).

To further assess the effect of integration scale, vector lines that track the measured ply angles can be overlaid on the phase data from which angles were measured. Three images from a region of interest are presented in Fig. 11 for the same three integration scales presented in Fig. 10.
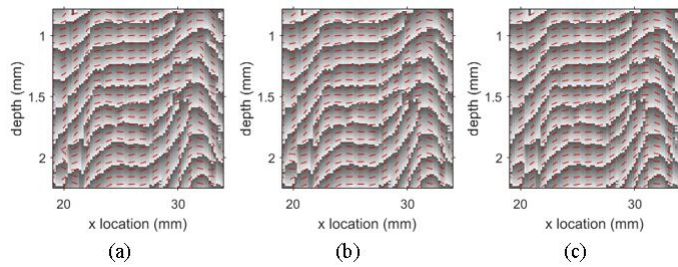

Figure 11: Vector lines overlaid on the phase data from which orientation was measured. Images show the effect of integration scale, τ, on the tracking-performance of the orientation measurement in a common cross-section. (a) $\tau = (0.2, 0.2, 0.012)$ mm, or $(1, 1, 1)$ pixels, (b) $\tau = (0.4, 0.4, 0.024)$ mm, or $(2, 2, 2)$ pixels, (c) $\tau = (1.0, 1.0, 0.061)$ mm, or $(5, 5, 5)$ pixels. The smoothing scale, σ, was set to zero (no smoothing) in all cases.

To generate the images in Fig. 11, vector lines have only been plotted at 1.0 mm spacing in the x-direction, and approximately 0.06 mm in the depth direction. For a large integration scale, Fig. 11(c), the measured orientation does not accurately reflect the underlying orientation in the data, tending to smooth out rapid changes in orientation, as expected. Whilst the smallest integration scale, Fig. 11(a), tracks the orientation better, it is affected by localised disruptions in the phase data, such as in the bottom-left of the image. The optimum integration scale, although a qualitative judgement, lies between these two values. At $\tau = (0.4, 0.4, 0.024)$ mm, Fig. 11(b), good tracking is observed with enough contribution from the surrounding area to keep the localised random phase-disruption effects to a minimum.

5.6. Correlation with real structure

It has been shown that, for the structure-tensor scale parameters selected as appropriate for this dataset ($\sigma = $ zero, $\tau = (0.4, 0.4, 0.024)$ mm, or $(2, 2, 2)$ pixels) the method is capable of generating a representative map of the wrinkled region to allow determination of wrinkle angle, wavelength and extent. It now remains to be determined if the measured orientations accurately reflect the ply wrinkling in the real structure. To achieve this, an X-ray CT image slice from the same location has been overlaid with vector lines from the structure-tensor analysis and presented in Fig. 12. In this figure the vector lines have only been plotted at depth locations predicted to be interfaces from the phase data (see Fig. 7). Additionally, vector lines are only plotted every 0.8 mm (4 pixels) in the x-direction. This reduces the quantity of data to a level where a visual assessment is possible, thus allowing a comparison of true orientation (greyscale X-ray CT image) with measured orientations (red vector lines).

Ideally, all vector lines should lie on the X-ray CT ply interfaces, and be oriented in the direction of the interface. Examination of the image in Fig. 12 reveals that the
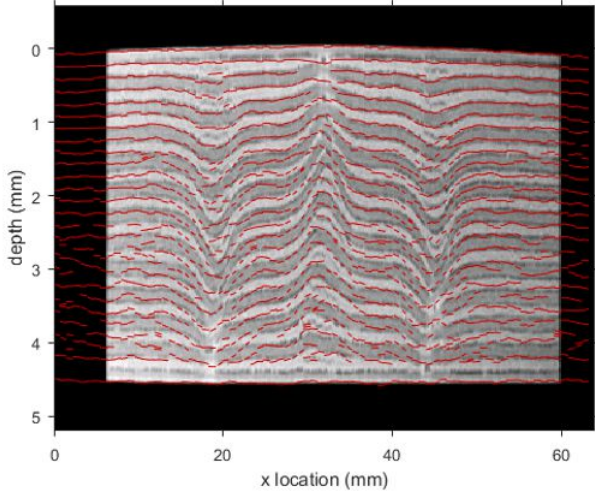
Figure 12: Correlation of measured and true orientations by overlaying vector lines of ply orientation measured from ultrasonic phase data on the X-ray CT image of the cross-section.

majority of interface locations are correctly located, and vector lines track their orientation. At deeper locations the phase-predicted interfaces are more frequently misaligned with the true structure, compared with near-surface locations where interface tracking is significantly better. This effect is demonstrated further in Fig. 13, which presents magnified views of the results in Fig. 12 to allow a more detailed visual inspection of the vector location and orientation at near-surface and far-surface locations, Fig. 13(a) and (b) respectively.
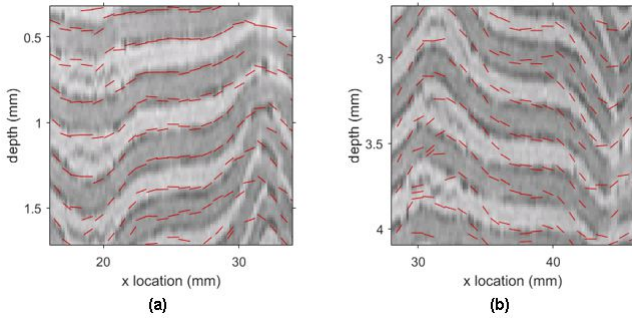

Figure 13: (a) Near surface and (b) far surface results of measured orientation (red vector lines) and real orientation (greyscale X-ray CT image).

Where the phase data fails to track the true ply structure at deeper locations, errors in the measured orientation

are more likely to occur. This is seen in Fig. 13(b), at an x-location of about 35 mm, and is thought to be largely a result of attenuation of the desired resonant frequency from the ultrasonic pulse, and typically coincides with tape gap/overlap locations. It is believed that, with improved processing of the raw ultrasonic waveform data, these effects can be reduced. Current work on waveform filtering, and the inclusion of other metrics, such as instantaneous frequency (rate of change of phase), suggest that improvements in this area are likely. It is also believed that the use of ultrasonic arrays, which allow raw data processing techniques such as multi-zone focusing and the total focussing method (TFM), will improve the raw waveform data and lead to an improvement in ply tracking and orientation measurement.

Even where vector lines do not lie directly at an interface, the orientation data in Fig. 13 is qualitatively correct. This is a substantial benefit since a key measurement to assess a CFRP laminate's compressive strength reduction due to ply wrinkling is the maximum wrinkle angle [3].

6. Summary and conclusions

This paper has demonstrated that ply wrinkling can be successfully characterised using ultrasonic instantaneous-phase datasets and structure-tensor angle-measurement methods. Ply-location analysis shows promise, but further work will be required to obtain the robust measurements needed for the generation of FE models.

New alignment and segmentation methods for ultrasonic-immersion scans have been presented. These use a precise phase-based measurement of the front-surface time-of-flight to correct for a tilted sample and for the different velocities in the water and composite, and then remove unwanted phase information from before and after the sample. This removes location errors that would otherwise be present using typical 'interface gating' methods, and

13

preserves curved-surface profiles and true ply orientations whilst aligning the data.

Methods to smooth the wrapped phase, and to calculate gradients directly from the wrapped phase, have been presented. These are critical to the structure-tensor process when working with wrapped-phase data, and allow accurate orientation information to be obtained without the high-gradient wrap locations dominating orientation results.

Investigations into the effect of the structure-tensor spatial scales identified that negligible smoothing is required, thus allowing the phase data to retain the high spatial-frequency components that accurately define the wrinkle. Unlike the smoothing scale, too small an integration scale leads to unnecessarily large local fluctuations and random errors, so a larger scale should be used. For the sample and data used in this paper, an integration-scale standard deviation of 0.4 mm has been shown to achieve good ply-orientation measurements from wrinkled regions, whilst a scale of 0.6 mm caused significant under-estimation of the maximum wrinkle angle.

At deeper depths and higher ply-orientation angles the phase data can become de-coupled from the ply structure, leading to errors in ply-location mapping and potential errors in the orientation measurement. This is thought to be a consequence of losing the desired resonant-frequency content in the ultrasonic pulse transmitted to the deeper layers, and the large number of tape gaps/overlaps. At locations closer to the front surface the structure-tensor technique applied to the phase data produces faithful measurements of the true orientation, as seen by comparing with the real structure, imaged using X-ray CT.

It is expected that improvement of the raw phase data with, for example, appropriate waveform filtering and advanced focussing techniques with array-based data acquisition, will generate higher-quality phase data and improve the accuracy of ply location and orientation measurement methods presented in this paper. These tools are then likely to become widely used for the detection and measurement of ply-wrinkling defects, and ply-location mapping, in carbon-fibre composite laminates.

References

[1] K. Potter, B. Khan, M. Wisnom, T. Bell, J. Stevens, Variability, fibre waviness and misalignment in the determination of the properties of composite materials and structures, Composites Part A: Applied Science and Manufacturing 39 (9) (2008) 1343–1354. doi:10.1016/j.compositesa.2008.04.016.

[2] M. Wisnom, The effect of fibre misalignment on the compressive strength of unidirectional carbon fibre/epoxy, Composites 21 (5) (1990) 403–407. doi:10.1016/0010-4361(90)90438-3.

[3] N. Xie, R. A. Smith, S. R. Hallett, Parametric study of the effect of out-of- plane wrinkles on compressive strength of composites Submitted for Publication.

[4] R. F. Elhajjar, S. S. Shams, G. J. Kemeny, G. Stuessy, A hybrid numerical and imaging approach for characterizing defects in composite structures, Composites Part A: Applied Science and Manufacturing 81 (2016) 98–104. doi:10.1016/j.compscitech.2012.08.009.

[5] G. Nikishkov, Y. Nikishkov, A. Makeev, Finite element mesh generation for composites with ply waviness based on X-ray computed tomography, Advances in Engineering Software 58 (2013) 35–44.

[6] G. Seon, Y. Nikishkov, A. Makeev, B. Shonkwiler, Mesh morphing methodology for strength predictions in composites,

Composite Structures 140 (2016) 612–620. `doi:10.1016/j.compstruct.2015.12.021`.

[7] R. Smith, L. Nelson, N. Xie, C. Fraij, S. Hallett, Progress in 3D characterisation and modelling of monolithic carbon-fibre composites, Insight-Non-Destructive Testing and Condition Monitoring 57 (3) (2015) 131–139. `doi:10.1784/insi.2014.57.3.131`.

[8] I. Straumit, S. V. Lomov, M. Wevers, Quantification of the internal structure and automatic generation of voxel models of textile composites from X-ray computed tomography data, Composites Part A: Applied Science and Manufacturing 69 (2015) 150–158. `doi:10.1016/j.compositesa.2014.11.016`.

[9] A. Bhattacharya, C. Heinzl, A. Amirkhanov, J. Kastner, R. Wenger, Metatracts-a method for robust extraction and visualization of carbon fiber bundles in fiber reinforced composites, in: 2015 IEEE Pacific Visualization Symposium (PacificVis), IEEE, pp. 191–198.

[10] J. Weissenböck, A. Amirkhanov, W. Li, A. Reh, A. Amirkhanov, E. Gröller, J. Kastner, C. Heinzl, Fiberscout: an interactive tool for exploring and analyzing fiber reinforced polymers, in: 2014 IEEE Pacific Visualization Symposium, IEEE, pp. 153–160. `doi:10.1109/PacificVis.2014.52`.

[11] M. Teßmann, S. Mohr, S. Gayetskyy, U. Haßler, R. Hanke, G. Greiner, Automatic determination of fiber-length distribution in composite material using 3D CT data, EURASIP Journal on Advances in Signal Processing 2010 (1) (2010) 1. `doi:10.1155/2010/545030`.

[12] O. Wirjadi, K. Schladitz, P. Easwaran, J. Ohser, Estimating fibre direction distributions of reinforced composites from tomographic images, Image Analysis & Stereology 35 (3) (2016) 167–179. `doi:10.5566/ias.1489`.

[13] J. Kastner, B. Plank, A. Reh, D. Salaberger, C. Heinzl, Advanced X-ray tomographic methods for quantitative characterisation of carbon fibre reinforced polymers, 4th International Symposium on NDT in Aerospace.

[14] V. Revol, B. Plank, R. Kaufmann, J. Kastner, C. Kottler, A. Neels, Laminate fibre structure characterisation of carbon fibre-reinforced polymers by X-ray scatter dark field imaging with a grating interferometer, NDT & E International 58 (2013) 64–71. `doi:10.1016/j.ndteint.2013.04.012`.

[15] Y. Sharma, M. Wieczorek, F. Schaff, S. Seyyedi, F. Prade, F. Pfeiffer, T. Lasser, Six dimensional X-ray tensor tomography with a compact laboratory setup, Applied Physics Letters 109 (13) (2016) 134102. `doi:10.1063/1.4963649`.

[16] J. Kastner, B. Plank, C. Kottler, V. Revol, Comparison of phase contrast X-ray computed tomography methods for non-destructive testing of materials, in: Conference Proceedings of the world conference on non-destructive testing, 2012.

[17] R. A. Smith, L. J. Nelson, M. J. Mienczakowski, P. D. Wilcox, Ultrasonic tracking of ply drops in composite laminates, in: AIP Conference Proceedings, Vol. 1706, AIP Publishing, 2016, p. 050006. `doi:10.1063/1.4940505`.

[18] L. J. Nelson, R. A. Smith, Three-dimensional fiber-orientation characterisation in monolithic carbon-fiber composites, in: Proc. European Conference on NDT, 2014.

[19] R. A. Smith, L. J. Nelson, M. J. Mienczakowski, R. E. Challis, Automated analysis and advanced defect characterisation from ultrasonic scans of composites, Insight-Non-Destructive Testing and Condition Monitoring 51 (2) (2009) 82–87.

[20] A. Sandhu, T. J. Dodwell, R. Butler, An autommated processing algorithm to determine wrinkle characteristics from B-scans, in: ECCM17 - 17th European Conference on Composite Materials, 2016.

[21] R. A. Smith, L. J. Nelson, M. Mienczakowski, P. D. Wilcox, Ultrasonic analytic-signal responses from polymer-matrix composite laminates, IEEE Transactions on Ultrasonics, Ferroelectrics, and Frequency Control, Accepted for publication (Oct. 2017).

[22] R. A. Smith, Use of 3D ultrasound data sets to map the localised properties of fibre-reinforced composites, Ph.d. (2010).

[23] R. Smith, L. Nelson, R. T. Boumda, N. Xie, C. Fraij, P. Wilcox, S. Hallett, Progress in nondestructive 3D characterization and modelling of aerospace composites, in: NDT of Composites II, ASNT, pp. 38–44.

[24] W. T. Freeman, E. H. Adelson, The design and use of steerable filters, IEEE Transactions on Pattern analysis and machine intelligence 13 (9) (1991) 891–906.

[25] E. P. Simoncelli, H. Farid, Steerable wedge filters for local orientation analysis, IEEE transactions on Image Processing 5 (9) (1996) 1377–1382.

[26] S. Paris, H. M. Briceño, F. X. Sillion, Capture of hair geometry from multiple images, in: ACM Transactions on Graphics (TOG), Vol. 23, ACM, 2004, pp. 712–719.

[27] O. Wirjadi, K. Schladitz, A. Rack, T. Breuel, Applications of anisotropic image filters for computing 2D and 3D-fiber orientations, in: Stereology and Image Analysis–10th European Congress of ISS.

[28] K. Schladitz, A. Büter, M. Godehardt, O. Wirjadi, J. Fleckenstein, T. Gerster, U. Hassler, K. Jaschek, M. Maisl, U. Maisl, Non-destructive characterization of fiber orientation in reinforced SMC as input for simulation based design, Composite Structures 160 (2017) 195–203. `doi:10.1016/j.compstruct.2016.10.019`.

[29] K. Robb, O. Wirjadi, K. Schladitz, Fiber orientation estimation from 3D image data: practical algorithms, visualization, and interpretation, in: 7th international conference on hybrid intelligent systems (HIS 2007), IEEE, pp. 320–325. `doi:`

10.1109/HIS.2007.26.

[30] S. Dietrich, J.-M. Gebert, G. Stasiuk, A. Wanner, K. Weidenmann, O. Deutschmann, I. Tsukrov, R. Piat, Microstructure characterization of CVI-densified carbon/carbon composites with various fiber distributions, Composites Science and Technology 72 (15) (2012) 1892–1900.

[31] G. Requena, G. Fiedler, B. Seiser, P. Degischer, M. Di Michiel, T. Buslaps, 3D-Quantification of the distribution of continuous fibres in unidirectionally reinforced composites, Composites Part A: Applied Science and Manufacturing 40 (2) (2009) 152–163. doi:10.1016/j.compositesa.2008.10.014.

[32] C. Creighton, M. Sutcliffe, T. Clyne, A multiple field image analysis procedure for characterisation of fibre alignment in composites, Composites Part A: Applied Science and Manufacturing 32 (2) (2001) 221–229.

[33] M. Sutcliffe, S. Lemanski, A. Scott, Measurement of fibre waviness in industrial composite components, Composites Science and Technology 72 (16) (2012) 2016–2023. doi:10.1016/j.compscitech.2012.09.001.

[34] K. K. Kratmann, M. Sutcliffe, L. Lilleheden, R. Pyrz, O. T. Thomsen, A novel image analysis procedure for measuring fibre misalignment in unidirectional fibre composites, Composites Science and Technology 69 (2) (2009) 228–238. doi:10.1016/j.compscitech.2008.10.020.

[35] C. Ayres, G. L. Bowlin, S. C. Henderson, L. Taylor, J. Shultz, J. Alexander, T. A. Telemeco, D. G. Simpson, Modulation of anisotropy in electrospun tissue-engineering scaffolds: analysis of fiber alignment by the fast Fourier transform, Biomaterials 27 (32) (2006) 5524–5534. doi:10.1016/j.biomaterials.2006.06.014.

[36] H. Heuer, M. Schulze, M. Pooch, S. Gäbler, A. Nocke, G. Bardl, C. Cherif, M. Klein, R. Kupke, R. Vetter, Review on quality assurance along the CFRP value chain–non-destructive testing of fabrics, preforms and CFRP by HF radio wave techniques, Composites Part B: Engineering 77 (2015) 494–501. doi:10.1016/j.compositesb.2015.03.022.

[37] M. Tunák, J. Antoch, J. Kula, J. Chvojka, Estimation of fiber system orientation for nonwoven and nanofibrous layers: local approach based on image analysis, Textile Research Journal 84 (9) (2014) 989–1006. doi:10.1177/0040517513509852.

[38] M. Krause, R. M. Alles, B. Burgeth, J. Weickert, Retinal vessel detection via second derivative of local Radon transform, Universitat des Saarlandes Technical Report No. 212. http://www.math.uni-sb.de/service/preprints/preprint212.pdf.

[39] B. B. Chaudhuri, P. Kundu, N. Sarkar, Detection and gradation of oriented texture, Pattern Recognition Letters 14 (2) (1993) 147–153.

[40] K. Jafari-Khouzani, H. Soltanian-Zadeh, Radon transform orientation estimation for rotation invariant texture analysis, IEEE Transactions on Pattern Analysis and Machine Intelligence 27 (6) (2005) 1004–1008.

[41] N. J. Schaub, S. J. Kirkpatrick, R. J. Gilbert, Automated methods to determine electrospun fiber alignment and diameter using the Radon transform, BioNanoScience 3 (3) (2013) 329–342. doi:10.1007/s12668-013-0100-y.

[42] M. Kass, A. Witkin, Analyzing oriented patterns, Computer vision, graphics, and image processing 37 (3) (1987) 362–385.

[43] A. Rao, B. Schunck, Computing oriented texture fields, in: Computer Vision and Pattern Recognition, 1989. Proceedings CVPR'89., IEEE Computer Society Conference on, IEEE, pp. 61–68.

[44] W. Förstner, E. Gülch, A fast operator for detection and precise location of distinct points, corners and centres of circular features, in: Proc. ISPRS intercommission conference on fast processing of photogrammetric data, 1987, pp. 281–305.

[45] J. Bigun, G. H. Granlund, Optimal orientation detection of linear symmetry, in: Proceedings of the IEEE First International Conference on Computer Vision, Linköping University Electronic Press, p. 433–438.

[46] H. Knutsson, Representing local structure using tensors, in: 6th Scandinavian Conference on Image Analysis, Oulu, Finland, Linköping University Electronic Press, 1989, pp. 244–251.

[47] L. J. Van Vliet, P. W. Verbeek, Estimators for orientation and anisotropy in digitized images, in: ASCI, Vol. 95, 1995, pp. 16–18.

[48] G. M. Van Kempen, N. van den Brink, L. J. van Vliet, M. Van Ginkel, P. W. Verbeek, H. Blonk, The application of a local dimensionality estimator to the analysis of 3-D microscopic network structures, in: Proceedings of the Scandinavian Conference on Image Analysis, Vol. 1, 1999, pp. 447–454.

[49] C.-F. Westin, S. E. Maier, H. Mamata, A. Nabavi, F. A. Jolesz, R. Kikinis, Processing and visualization for diffusion tensor MRI, Medical image analysis 6 (2) (2002) 93–108.

[50] M. Krause, J.-M. Hausherr, B. Burgeth, C. Herrmann, W. Krenkel, Determination of the fibre orientation in composites using the structure tensor and local X-ray transform, Journal of Materials Science 45 (4) (2010) 888. doi:10.1007/s10853-009-4016-4.

[51] M. Axelsson, Estimating 3D fibre orientation in volume images, in: Pattern Recognition, 2008. ICPR 2008. 19th International Conference on, IEEE, 2008, pp. 1–4.

[52] Z. Yu, C. Bajaj, A structure tensor approach for 3D image skeletonization: Applications in protein secondary structure analysis, in: Image Processing, 2006 IEEE International Conference on, IEEE, pp. 2513–2516.

[53] R. S. J. Estépar, Local structure tensor for multidimensional sig-

nal processing: applications to medical image analysis, Presses univ. de Louvain, 2007.

[54] X. Wu, D. Hale, 3D seismic image processing for unconformities, Geophysics 80 (2) (2015) IM35–IM44. `doi:10.1190/GEO2014-0323.1`.

[55] X. Wu, X. Janson, Directional structure tensors in estimating seismic structural and stratigraphic orientations, Geophysical Journal International 210 (1) (2017) 534–548. `doi:10.1093/gji/ggx194`.

[56] R. A. Smith, L. J. Nelson, M. J. Mienczakowski, Phononic band gaps and phase singularities in the ultrasonic response from toughened composites., in: 2017 Review of Progress in Quantitative NDE, AIP Publishing, 2018.

[57] P.-H. B. Jonathan, J. Kratz, O. J. Nixon-Pearson, T. Mesogitis, D. S. Ivanov, S. R. Hallett, Predicting wrinkle formation in components manufactured from toughned UD prepreg., ECCM17 - 17th European Conference on Composite Materials.